Ultra-compact Integrated Silicon Photonics Balanced Coherent Photodetectors

Item type	text; Electronic Thesis
Authors	Meyer, Jason T.
Publisher	The University of Arizona.
Rights	
Downloaded	
Link to item	http://hdl.handle.net/10150/613424

ULTRA-COMPACT INTEGRATED SILICON PHOTONICS BALANCED COHERENT PHOTODETECTORS

by

Jason T. Meyer

A Thesis Submitted to the Faculty of the

COLLEGE OF OPTICAL SCIENCES

In Partial Fulfillment of the Requirements

For the Degree of

MASTER OF SCIENCE

In the Graduate College

THE UNIVERSITY OF ARIZONA

2016

STATEMENT BY AUTHOR

The thesis titled “Ultra-compact Integrated Silicon Photonics Balanced Coherent Photodetectors” prepared by Jason T. Meyer has been submitted in partial fulfillment of the requirements for a master’s degree at the University of Arizona and is deposited in the University Library to be made available to borrowers under the rules of the Library.

Brief quotations from this thesis are allowable without special permission, provided that an accurate acknowledgement of the source is made. Requests for permission for extended quotation from or reproduction of this manuscript in whole or in part may be granted by the head of the major department or the Dean of the Graduate College when in his or her judgment the proposed use of the material is in the interests of scholarship. In all other instances, however, permission must be obtained from the author.

SIGNED: ____________________

Jason T. Meyer

APPROVAL BY THESIS DIRECTOR

This thesis has been approved on the date shown below:

__________________________ April 28th, 2016

Mahmoud Fallahi
Professor of Optical Sciences

Date

ACKNOWLEDGEMENTS

First, I would like to thank my advising professor, Dr. Mahmoud Fallahi, for providing me with the research opportunity that led to this thesis work. His patience, guidance, and encouragement helped create the student that I am today.

I would also like to acknowledge Michal Lukowski, a doctoral student in Dr. Fallahi's research group, for spending a large part of his time teaching me how to fabricate optical devices. You have my gratitude, and my never-ending series of questions.

A special thank you also goes to Dr. Lonnie Burke and Dr. Anthony Pitucco, professors of chemistry and physics, respectively. Early on in my academic career, they were pivotal in developing my integrity as a student and provided me with the invaluable opportunity to tutor other students. I am here because of you, and speak often of your teaching methodologies.

Finally, I would like to thank my partner, Jessica Normoyle, for standing by me and supporting me through the last few years. I would not be in graduate school pursuing my academic goals without you. Thank you for believing in me.

TABLE OF CONTENTS

ABSTRACT

The design, simulation, and initial fabrication of a novel ultra-compact 2x2 silicon multimode-interference (MMI) device evanescently coupled to a dual germanium metal-semiconductor-metal (MSM) photodetector is presented. For operation at the standard telecom wavelength of 1.5 µm, the simulations demonstrate high-speed operation at 30 GHz, low dark current in the nanoamp range, and external quantum efficiency of 80%. Error analysis was performed for possible tilt error introduced by hybrid integration of the MSM layer on top of the MMI waveguides by use of surface mount technology (SMT) and direct wafer bonding.

1. INTRODUCTION AND RESEARCH OBJECTIVES

The rapid expansion of the Internet in recent years has led to an increase in demand and capacity of the telecommunications infrastructure. Conventional technology utilizing typical copper interconnects have a limited data rate and increasing power consumption [Makoto Miura]. Silicon photonics has emerged as a promising new technology, offering optoelectronic solutions that lower cost, increase bandwidth, and lower power consumption of many telecommunication applications while being compatible with modern CMOS technology [1-3]. Novel devices using germanium have gained popularity due to the low cost of integration and its band gap of 0.8 eV, which allows for absorption of wavelengths around 1.5 µm, a standard in the telecommunications industry [4]. However, the large lattice mismatch that exists between germanium and silicon presents challenges for epitaxial growth, requiring specialized techniques to avoid defects between the silicon and germanium layers [4-6].

Our approach to solving these challenges was to design an ultra-compact coherent balanced 2x2 multimode interference (MMI) device that would be evanescently (vertically) coupled to a germanium metal-semiconductor-metal (MSM) photodetection layer for signal extraction [7-8]. While metal-semiconductor-metal (MSM) photodetection is not a new technology, it is ideal for use in ultra-compact devices due to its ability to offer low capacitance leading to high bandwidth, simplicity in fabrication, and low cost [1, 8, 9]. Finally, evanescent coupling from the silicon waveguides to the germanium photodetection layer allows for separate fabrication of the MMI and MSM. This enables us to use hybrid integration and direct wafer bonding techniques to bond the germanium MSM to the silicon MMI, effectively avoiding epitaxial growth issues [6].

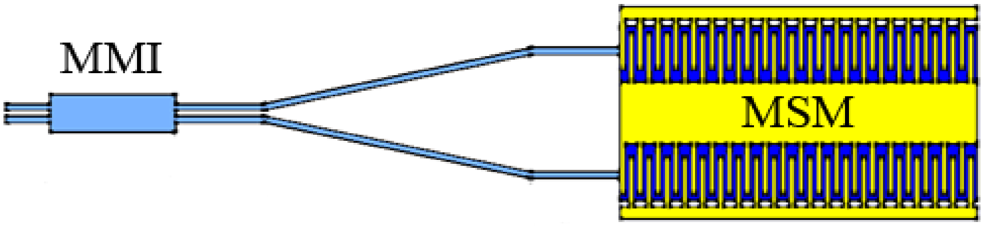

Figure 1.1. Top-down view of the proposed MMI to MSM photodetector structure.

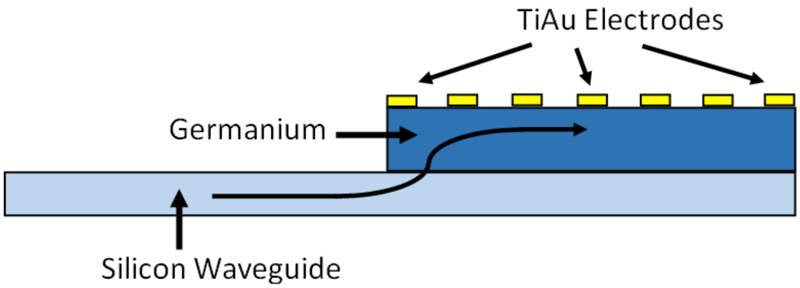

Figure 1.2. Profile view of the proposed device.

Coherent detection has become an area of increased interest due to its ability to increase capacity through maximizing spectral efficiency of wave division multiplexing, enabling polarization multiplexing, and utilizing digital signal processing techniques to reduce transmission impairments [10, 11]. In coherent detection schemes, the phase information of the signal is able to be extracted. This is different than direct detection schemes, where phase information is usually lost [10]. Balanced coherent detection has the added bonus of being able to almost entirely suppress the local oscillator relative intensity noise, while requiring less power to operate than single detector schemes [12]. This results in a very efficient, low-power coherent photodetector solution.

2. DESIGN AND SIMULATION OF WAVEGUIDES AND MMI DEVICE

2.1. Waveguides

For compatibility with modern CMOS devices, we selected commercially available silicon-on-insulator (SOI) structures as the waveguide system due to its low loss at standard telecom wavelengths of 1.5 µm, ease of fabrication, and low cost [2]. For single mode propagation, a typical slab waveguide geometry has a width of 0.5 µm and a height of 0.22 µm. The single mode profiles for TE and TM fields at 1.5 µm are shown below in Figure 2.1 and Figure 2.2, respectively, as simulated using Optiwave OPTIBPM software.

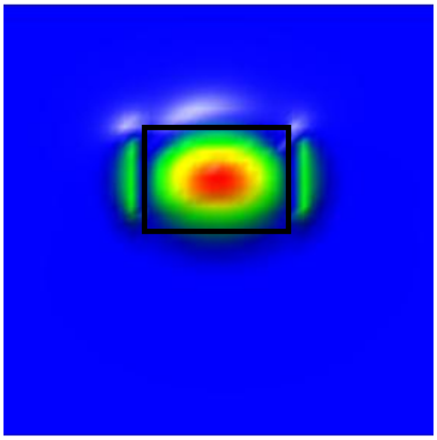

Figure 2.2. Single mode profile for the TE field in the silicon waveguide.

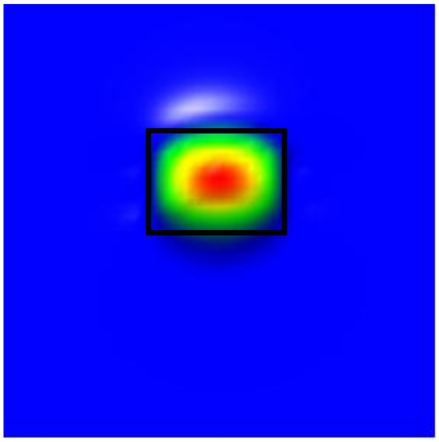

Figure 2.2. Single mode profile for the TM field in the silicon waveguide.

2.2. MMI Design

A multimode interference device (MMI) is a waveguide structure that is usually designed to support a large number of modes [7]. The functionality of the device is based on the optical self-imaging principle, which is simply "a property of multimode waveguides by which an input field profile is reproduced in single or multiple images at periodic intervals along the propagation direction of the guide" [7]. In other words, a central waveguide structure takes 1xN input waveguide signals, mixes (interferes) them, and then splits the mixed signal down 1xM output waveguides. At specific intervals along the propagation length of the MMI device, the coupled (mixed) image of the 1xN input signals will be split equally in power down the 1xM output waveguides. For restricted interference, where only certain modes in the MMI are excited by the input fields, this interval length is given by [7]

$$L = \frac{p}{N} L_\pi \tag{2.1}$$

with

$$L_\pi \cong \frac{4 n_r W_e^2}{3\lambda_0} \tag{2.1}$$

$$W_e \cong W_M + \left(\frac{\lambda_0}{\pi}\right)\left(\frac{n_c}{n_r}\right)^{2\sigma} (n_r^2 - n_c^2)^{-1/2} \tag{2.2}$$

where L_π is the beat length of the two lowest-order modes and W_e is the effective width of the MMI device. The remaining variables in equations (2.1)-(2.2) can be observed in Table 1, below.

Variable	Description	Value
n_r	Ridge Index	3.48
n_c	Cladding Index	1.0
W_M	Width of MMI	3.0 µm
λ_0	Wavelength	1.5 µm
σ	Varies based on Input Field	0 for TE, 1 for TM
p	Self-Image Iteration	1
N	Number of Outputs	2

Table 1. Properties and descriptions for MMI modeling.

In our balanced detection approach, we will use two input waveguide ports: one for the signal of interest and one for the local oscillator. After these signals are coupled, we want the total signal power to be divided in half, which each half being output down its own waveguide. The length of MMI needed to accomplish this was calculated to be approximately 14.83 µm. Using this length, we again used OPTIBPM simulation software to model the single mode propagation through this device. The simulation results are shown in Figure 2.3.

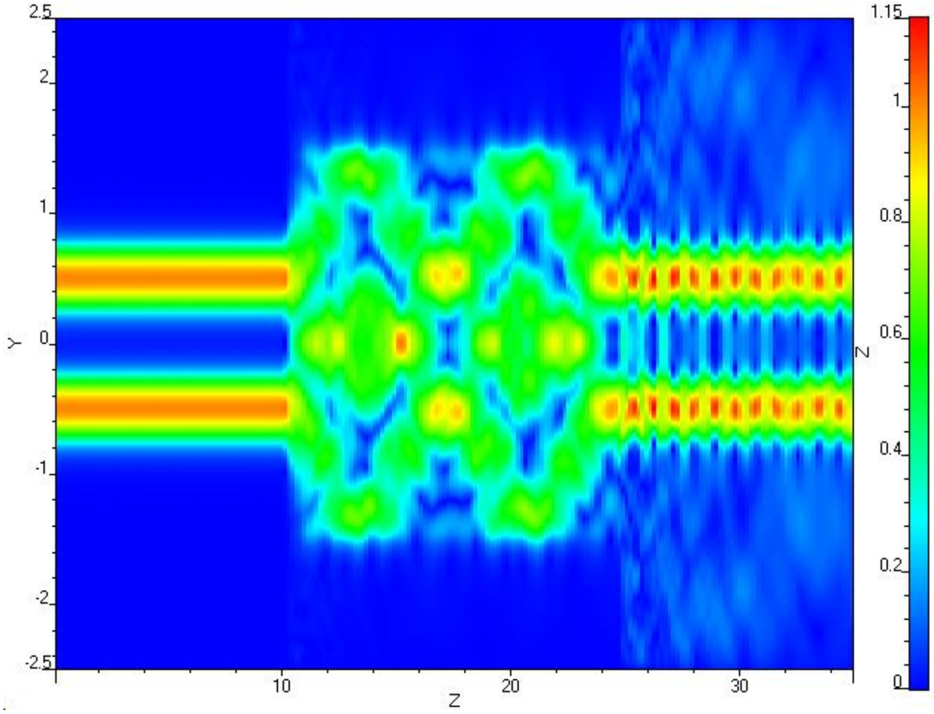

Figure 2.3 Single mode propagation simulation through 2x2 MMI with an MMI length of 14.83 µm.

The simulation does show that we do obtain self-imaging of the inputs with an MMI length of 14.83 µm. However, the output fields are rather messy with rapid fluctuations in amplitude. If we adjust the length of the MMI in the simulation from 14.83 µm to 14.6 µm, a difference of 1.6%, we obtain much cleaner field output, as shown in Figure 2.4.

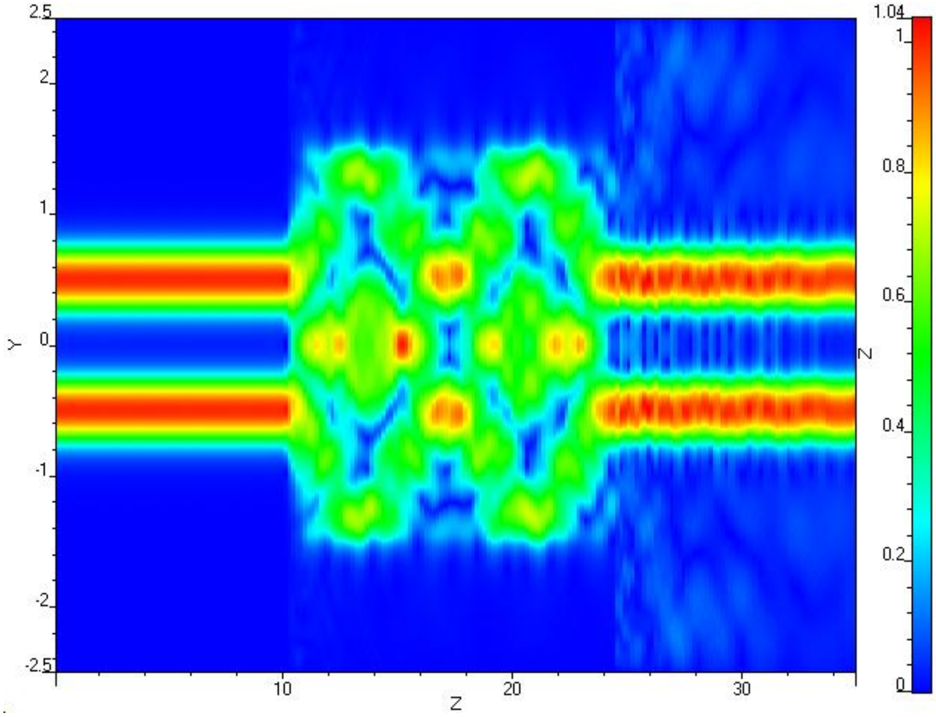

Figure 2.4. Single mode propagation simulation through 2x2 MMI with an MMI length of 14.6 µm.

3. DESIGN AND SIMULATION OF MSM

The metal-semiconductor-metal (MSM) photodetector is a device that has been widely used for detection schemes for a few decades due to its simplicity. With modern fabrication equipment and techniques, these devices can be made ultra-compact, which in turn leads to its ability to offer extremely low capacitance, high bandwidth, and low cost [1, 8, 9]. Furthermore, the MSM is a geometrically simple device from a design standpoint, consisting of a repetitive pattern of metal electrode fingers deposited on top of a bulk semiconductor layer. This makes fabrication relatively easy [8].

3.1. External Quantum Efficiency

The external quantum efficiency of the waveguide photodetector is dependent on both the detection length as well as the confinement factor and can be defined by [13]

$$\eta_{WGPD} = 1 - e^{-\alpha\Gamma L} \tag{3.10}$$

where α is the absorption coefficient, Γ is the confinement factor, and L is the length of the waveguide. If we assume a typical range for confinement factor of 0.075-0.125 and using 4000 cm^{-1} for the absorption coefficient of germanium, we will be able to obtain approximately 80% quantum efficiency with an MSM photodetector length of 40 µm and a confinement factor of 0.10, as shown in Figure 3.1.

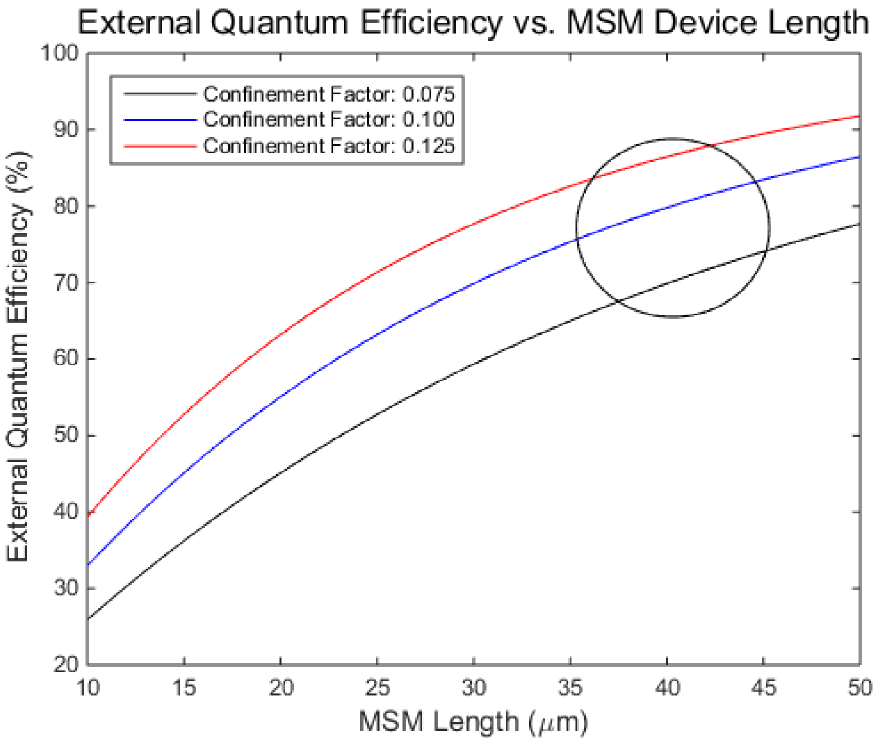

Figure 3.1. External quantum efficiency for an MSM device length of 10-50 µm using an absorption coefficient of 4000 cm^{-1}.

This performance is excellent as we want to maintain the ultra-compactness of the overall device. We could continue to increase the length of the photodetector to increase the external quantum efficiency to 90% or even 100%, but due to its exponential nature, it would take significantly more length for less and less return in efficiency gain.

It is important to note that the absorption coefficient of germanium declines rapidly around the 1.55 µm wavelength region. As aforementioned, the approximate value for the absorption coefficient of germanium of 1.5 µm is 4000 cm^{-1} but drops to approximately 400 cm^{-1} at 1.55 µm. If we re-plot the external quantum efficiency using this lower absorption coefficient, we obtain the plot seen in Figure 3.2.

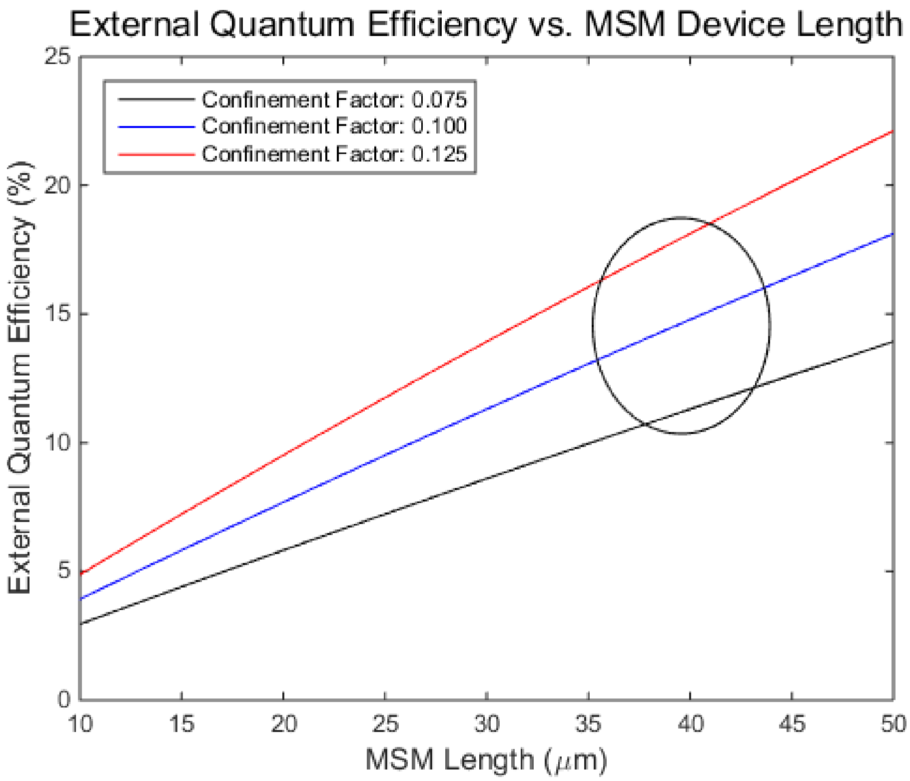

Figure 3.2. External quantum efficiency for an MSM device length of 10-50 µm using an absorption of 400 cm^{-1}.

The reduction in absorption coefficient has drastically reduced the efficiency of the MSM at 40 µm from 80% to roughly 15%. We would have to increase the length of the MSM to 400 µm in order to gain 80% efficiency using a wavelength of 1.5 µm. This underscores the importance of the proper wavelength operating region in order to maximize the efficiency of the device while maintaining its ultra-compact size. If wavelength division multiplexing is utilized, different wavelengths will experience different levels of quantum efficiency, thus affecting device performance. This will be tied into the total output photocurrent, which will be discussed later.

3.2. Responsivity

The responsivity of the MSM photodetector is the ratio of the generated photocurrent to the input optical power and can be modeled as [14]

$$R = \left|\frac{I_{ph}}{P_{inc}}\right| = \frac{q\eta_{WGPD}}{h\nu} = \frac{\lambda\eta_{WGPD}}{1.24}\ (A/W) \tag{3.11}$$

where λ is our wavelength in microns, η_{WGPD} is the external quantum efficiency of our waveguide photodetector given by (3.10), q is the electron charge, h is Planck's constant, and ν is the optical frequency. If we employed a more typical device using surface illumination photodetection (SIPD), we would also need to take into account the effect of electrode shadowing and reflection at the interface, which would reduce the amount of incident optical power that can penetrate into the semiconductor. However, evanescent coupling effectively eliminates this issue with the primary constraint on performance being that of confinement factor. As shown in Figure 3.3, we can achieve a responsivity of approximately 0.9 A/W with a photodetector length of 40 µm. This is in general agreement with [15-16].

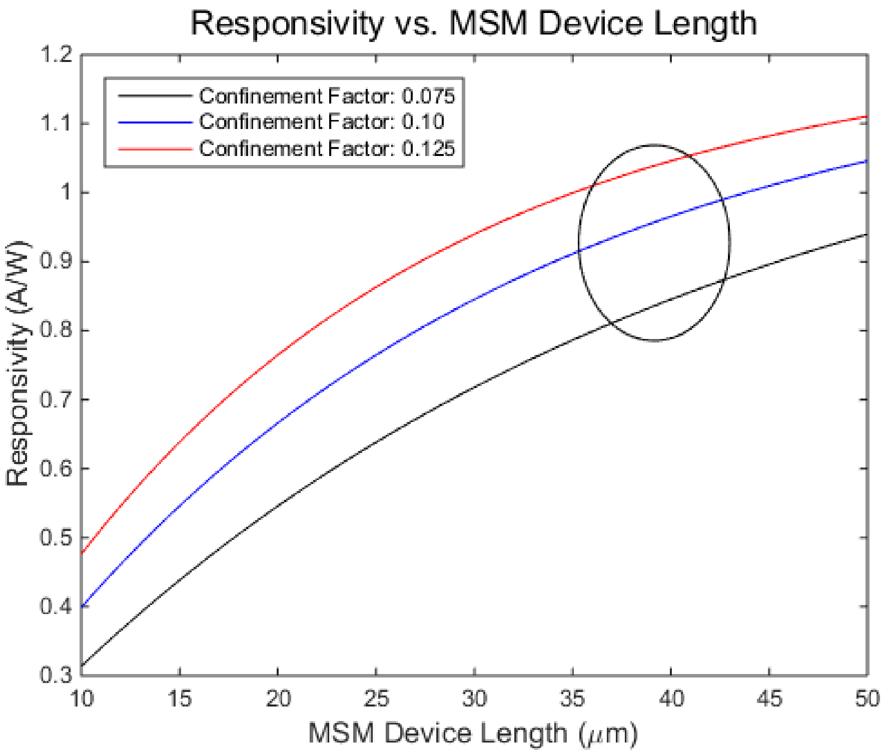

Figure 3.3. Responsivity vs. MSM device length between 10-50 μm for confinement factors of 0.075, 0.10, and 0.125. This was using an absorption coefficient of 4000 cm^{-1}.

As aforementioned in section 3.2, the external quantum efficiency is highly dependent on the absorption coefficient of the semiconductor material, which is itself dependent on the operating wavelength. It is immediately clear from equation (3.11) that the responsivity is similarly connected to the absorption coefficient. As shown in Figure 3.4, if the absorption coefficient drops from 4000 cm^{-1} to 400 cm^{-1}, the responsivity drops to approximately 0.16 A/W. Again, this underscores the importance of using an appropriate operating wavelength.

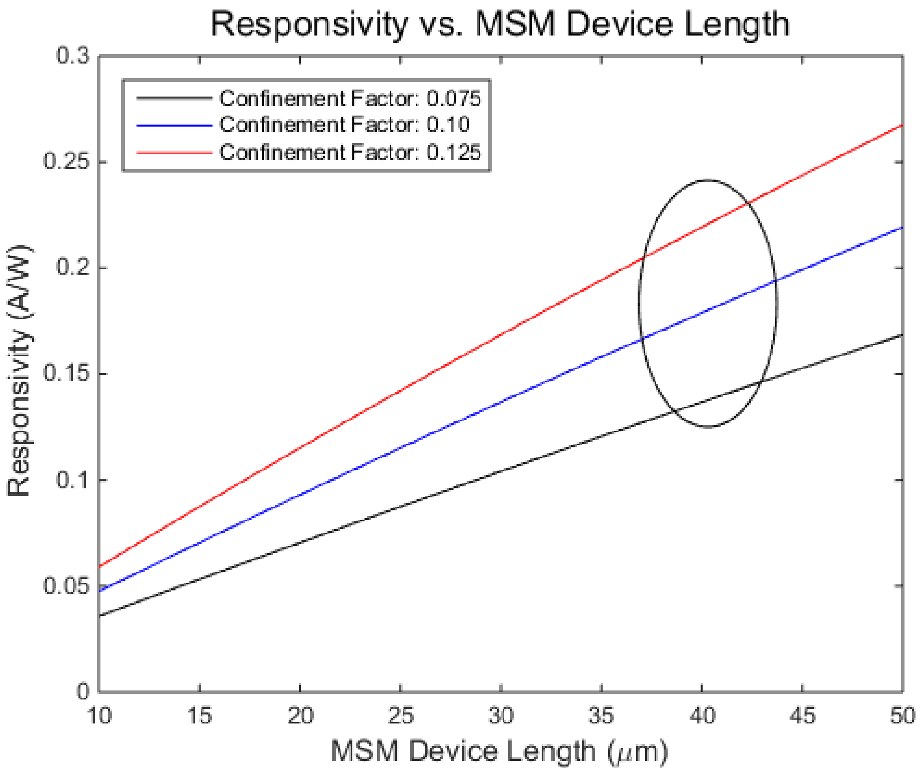

Figure 3.4. Responsivity vs. MSM device length between 10-50 µm for confinement factors of 0.075, 0.10, and 0.125. This is using an absorption coefficient of 400 cm^{-1}.

3.3. Dark Current

When a metal comes in contact with a semiconductor, a metal-semiconductor contact is formed. As was mentioned in section 2.2, a MSM photodetector is simply two Schottky contacts formed on either side of an undoped semiconductor. When bias voltage is applied across this metal-semiconductor-metal interface, one metal will be reverse biased while the other will be forward biased. Electrons trying to move from the reverse biased metal into the semiconductor will see a potential barrier φ_n (also known as the Schottky barrier) while the holes moving from the forward biased metal into the semiconductor will see a potential barrier φ_p. The summation of these two potential barriers will be equal to the bandgap of the semiconductor. In the case of germanium, with a bandgap of 0.66 eV, the typical barrier height φ_n is approximately 0.50 eV. This results in a hole barrier height of approximately 0.16 eV. Due to this low barrier height for holes, we would expect that the dark current will be dominated by thermionic emission of holes over this barrier.

For voltages larger than the flatband voltage, we can model the dark current using the equation given by [8]

$$J = A_n^* T^2 \exp\left\{-\frac{e(\varphi_n - \Delta\varphi_n)}{kT}\right\} + A_p^* T^2 \exp\left\{-\frac{e(\varphi_p - \Delta\varphi_p)}{kT}\right\} \tag{3.1}$$

where $\Delta\varphi_n$ and $\Delta\varphi_p$ are the image force lowering effects for electrons and holes, and A_n^* and A_p^* are the effective Richardson constants for electrons and holes. The image force lowering effect can be modeled as [8]

$$\Delta\varphi_{n,p} = \sqrt{\frac{eV}{4\pi\epsilon L}} \tag{3.2}$$

where V is the applied voltage, ϵ is the relative permittivity of the semiconductor, and L is the separation between the metal contacts.

For a germanium semiconductor with TiAu electrode fingers separated by 500 nm, the dark current will be in the 0.5 mA range, demonstrated in Figure 3.5, as was expected due to the low hole barrier height. However, barrier enhancement techniques exist to increase the Schottky barrier by isolating the contact pads and electrode fingers on a silicon nitride layer [17], or inserting a silicon-carbon (Si:C) barrier enhancement layer between the metal and germanium interface [18]. Research into the latter has demonstrated an enhanced hole barrier height of approximately 0.52 eV. Using this approximation, we can reduce dark current to the low nanoamp range, as shown in Figure 3.6.

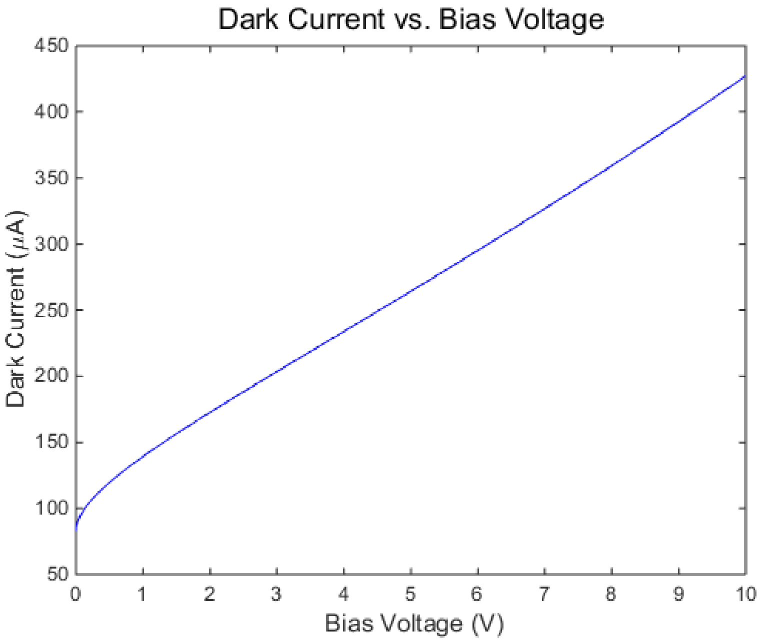

Figure 3.5. Dark current vs. bias voltage for a barrier hole height of 0.16 eV.

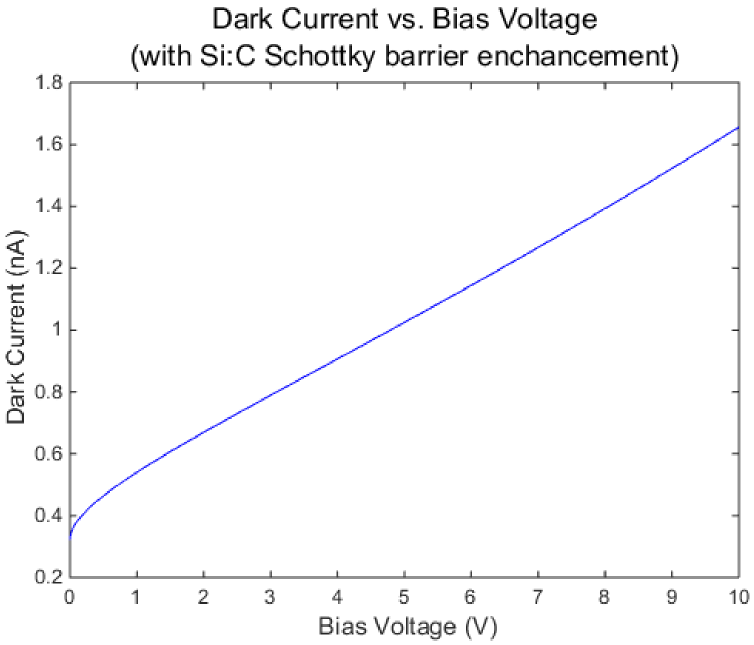

Figure 3.6. Dark current vs. bias voltage for an enhanced barrier hole height of 0.52 eV.

3.4. Capacitance

The photodetector should also be fast enough for modern optical communication systems in networking environments. This necessitates capacitance to be as low as possible in order to achieve operation in the GHz regime. For the MSM with interdigitated electrodes, the capacitance is given by [8]

$$C = \frac{K(k)}{K(k')}\epsilon_0(1+\epsilon_r)\frac{A}{finger\,period} \tag{3.3}$$

where $K(k)$ is the complete elliptic integral of the first kind, A is the detector area, and ϵ_r is the relative permittivity of the semiconductor. We can find k and k' from

$$k = \tan^2\left\{\frac{\pi(finger\,width)}{4(finger\,period)}\right\} \tag{3.4}$$

and

$$k' = \sqrt{1-k^2} \tag{3.5}$$

where the finger width and finger period are 0.5 µm and 1.0 µm, respectively. If we select a finger length of 4 µm, we obtain the plot shown in Figure 3.7 for a device length of 10-50 µm. With a MSM photodetector length of 40 µm, we will still be operating in a very low femtofarad capacitance region while also maintaining the ultra-compactness of the device. However, a device length slightly larger or smaller than 40 µm does not result in a dramatic change in capacitance. This would give us great flexibility in photodetector length if we were not already restricted by external quantum efficiency and responsivity issues.

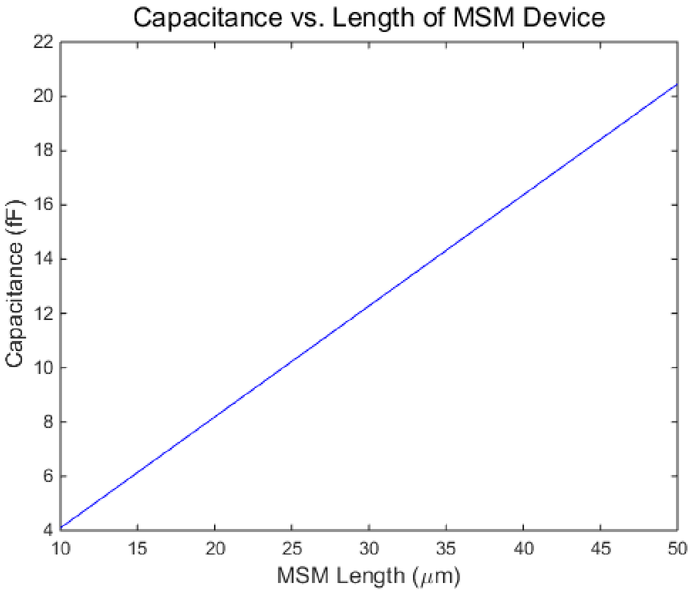

Figure 3.7. Capacitance vs. length of MSM between 10 and 50 μm.

We can also determine the capacitance as a function of voltage from [19]

$$C = \frac{C_0}{\left(1 - \frac{V_r}{V_{bi}}\right)^m} \tag{3.6}$$

where C_0 is the capacitance at zero voltage given by (3.3), V_{bi} is the built-in potential (or contact potential), V_r is the voltage across the reverse-biased region and is determined by the difference between the built-in potential and the total positive applied voltage, and m is the junction capacitance grading coefficient. As shown in Figure 3.8, as the voltage is increased, we see a gradual reduction in the capacitance.

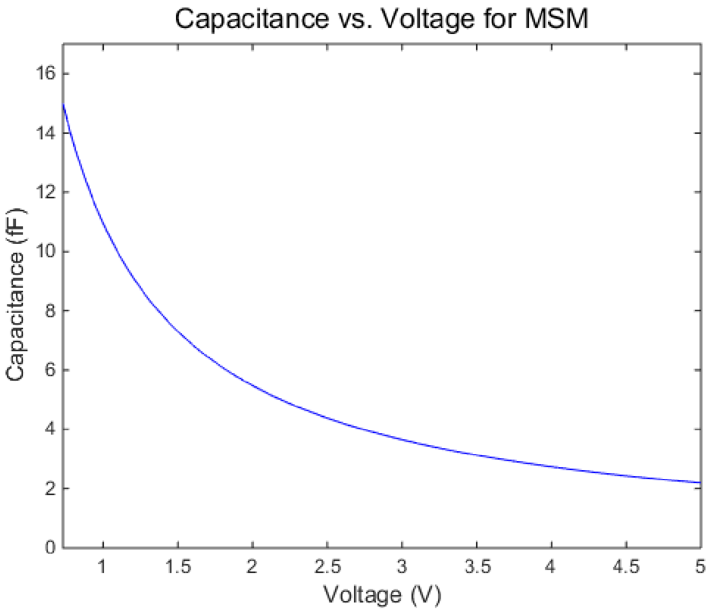

Figure 3.8. Capacitance of MSM device for a bias voltage up to 5 V. The length of the MSM was fixed at 40 µm.

3.5. 3-dB Optical Frequency

For the MSM photodetector, the 3-dB frequency can be determined by [20]

$$f_{3dB} \cong \frac{1}{2\pi\sqrt{(t_{tr})^2 + (RC)^2}} \tag{3.7}$$

with t_{tr}, the carrier transit time, defined as

$$t_{tr} = \frac{1}{2}\frac{L}{v_s}\eta \tag{3.8}$$

where R is the load resistance, C is the MSM capacitance, L is the spacing between electrode fingers, v_s is the carrier drift velocity, and η is a corrective constant (assumed to be unity). With t_{tr}>>RC, equation (3.7) simplifies to

$$f_{3dB} \cong \frac{v_s}{\pi L} \tag{3.9}$$

which demonstrates that the cutoff frequency of the MSM photodetector has a strong dependence on the carrier drift velocity (which is itself dependent on the applied voltage) and the spacing between electrode fingers. These relationships can be observed in Figure 3.9 and Figure 3.10.

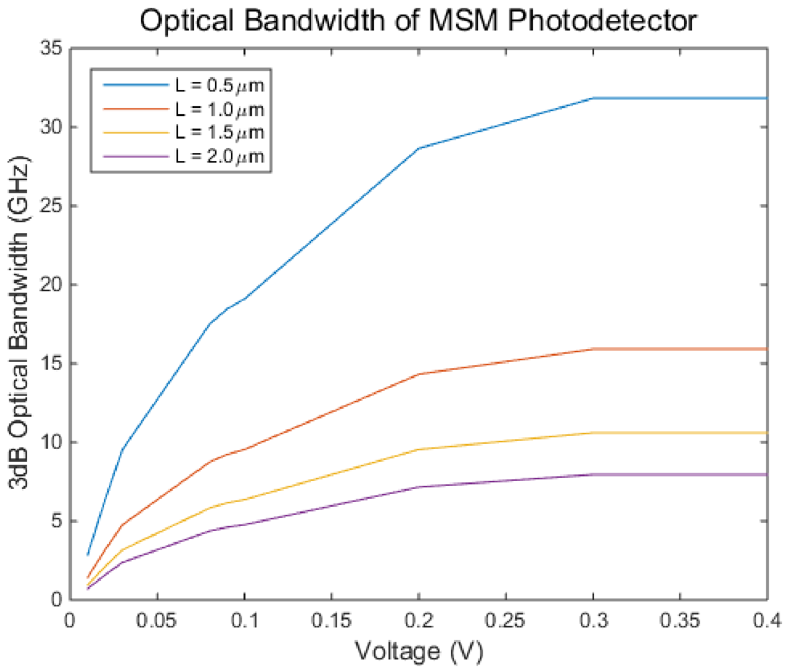

Figure 3.9. 3-dB optical bandwidth of MSM photodetector for a voltage up to 0.4 V. Note that saturation occurs after 0.4 V.

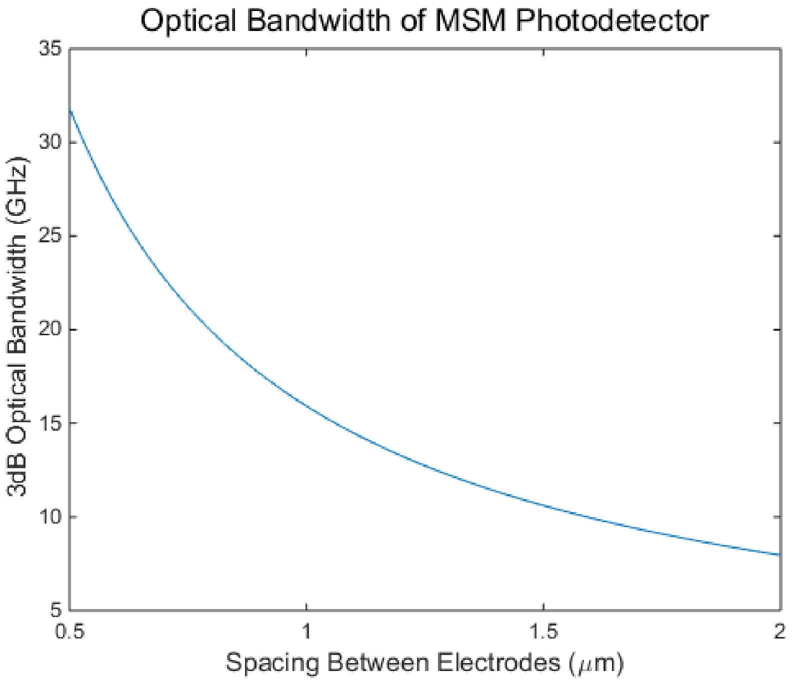

Figure 3.10. 3-dB optical bandwidth of MSM photodetector as a function of interdigitated electrode spacing.

3.6. Evanescent Coupling Between Silicon and Germanium Layers

With an MSM photodetector length set to be 40 µm, we used OPTIBPM simulation software to verify proper evanescent coupling from the silicon waveguide to the germanium photodetection layer. The optical signal was propagated along the silicon waveguide for 20 µm before encountering the germanium photodetector layer. As can be observed in Figure 3.11, the optical signal begins to evanescently couple from the silicon layer into the germanium layer almost immediately after the 20 µm mark.

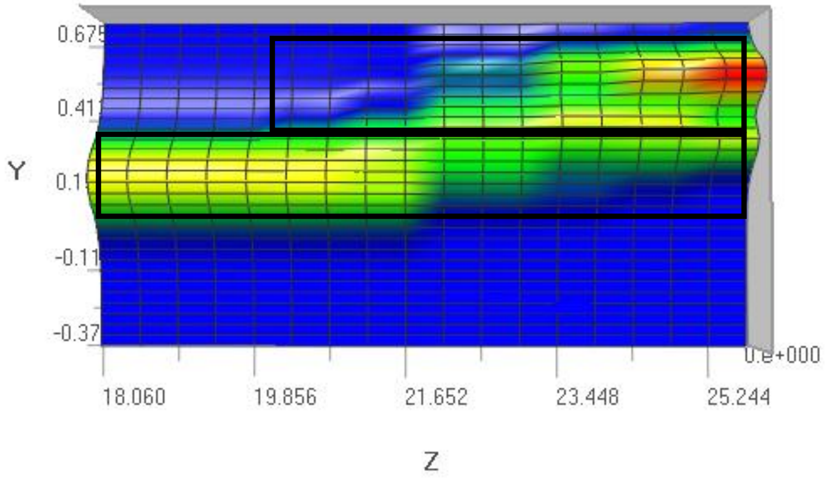

Figure 3.11. Evanescent coupling of the signal from the silicon waveguide (bottom rectangle) into the germanium photodetector layer (top rectangle).

4. PRIMARY SOURCES OF ERROR

The MMI-MSM device will be fabricated as two separate structures. First, the MMI device would be fabricated in-situ. Utilizing surface mount technology (SMT), the pre-fabricated MSM device would be placed directly over the output waveguides. This method of hybrid integration would take advantage of direct wafer bonding to bypass complicated epitaxial growth issues that would arise from growing germanium on silicon. However, this would lead to possible tilt error introduced by incorrect placement of the MSM photodetector over the output waveguides by the SMT device. This necessitates the characterization of this possible error to understand when integrity of the mixed single phase is compromised.

4.1. MSM Layer Tilt

As mentioned in section 2.2, the 2x2 MMI to MSM balanced coherent photodetector functions by coupling an incoming optical signal of interest with a local oscillator inside a multimode interference device. After coupling, the signal power is split in half and output down two symmetric silicon waveguides. The optical power in each output waveguide can be expressed as [10]

$$P_1 = \frac{P_s}{2} + \frac{P_{LO}}{2} + \sqrt{P_s P_{LO}} \cos[(\omega_s - \omega_{LO})t + \varphi_s - \varphi_{LO}] \tag{4.1}$$

$$P_2 = \frac{P_s}{2} + \frac{P_{LO}}{2} - \sqrt{P_s P_{LO}} \cos[(\omega_s - \omega_{LO})t + \varphi_s - \varphi_{LO}] \tag{4.2}$$

where P_s, ω_s, and ϕ_s are the signal power, frequency, and phase, respectively. Similarly, P_{LO}, ω_{LO}, and ϕ_{LO} are the local oscillator power, frequency, and phase, respectively.

A germanium layer, bonded on top of the silicon waveguides, will allow for evanescent coupling of the optical signal from the silicon waveguides into the germanium photodetector. Interdigitated TiAu Schottky electrodes placed on top of the germanium layer can then extract photocurrent from the optical signals. These photocurrents can be expressed as

$$I_1 = \frac{I_s}{2} + \frac{I_{LO}}{2} + R\sqrt{P_s P_{LO}}\cos[(\omega_s - \omega_{LO})t + \varphi_s - \varphi_{LO}] \tag{4.3}$$

$$I_2 = \frac{I_s}{2} + \frac{I_{LO}}{2} - R\sqrt{P_s P_{LO}}\cos[(\omega_s - \omega_{LO})t + \varphi_s - \varphi_{LO}] \tag{4.4}$$

where R, I_s, and I_{LO} are the responsivity of the photodetector, signal photocurrent, and local oscillator photocurrent, respectively. The balanced nature of the photodetector will result in the subtraction of I_2 from I_1, which will lead to the expression

$$I_1 - I_2 = 2R\sqrt{P_s P_{LO}}\cos[(\omega_s - \omega_{LO})t + \varphi_s - \varphi_{LO}]. \tag{4.5}$$

Since our photodetector is operating as a heterodyne receiver, the local oscillator and signal frequencies will be approximately the same. This results in the expression

$$I = I_1 - I_2 = 2R\sqrt{P_s P_{LO}}\cos[\varphi_s - \varphi_{LO}]. \tag{4.6}$$

It is now apparent that the output photocurrent will fluctuate sinusoidally with a change in the phase of the signal or local oscillator. However, all of this assumes that the germanium photodetector layer is bonded perfectly to the silicon waveguides (see Figure 4.1). A more realistic model will assume that there will be some amount of tilt (see Figure 4.2) of the germanium layer, resulting in phase error within our cosine term above.

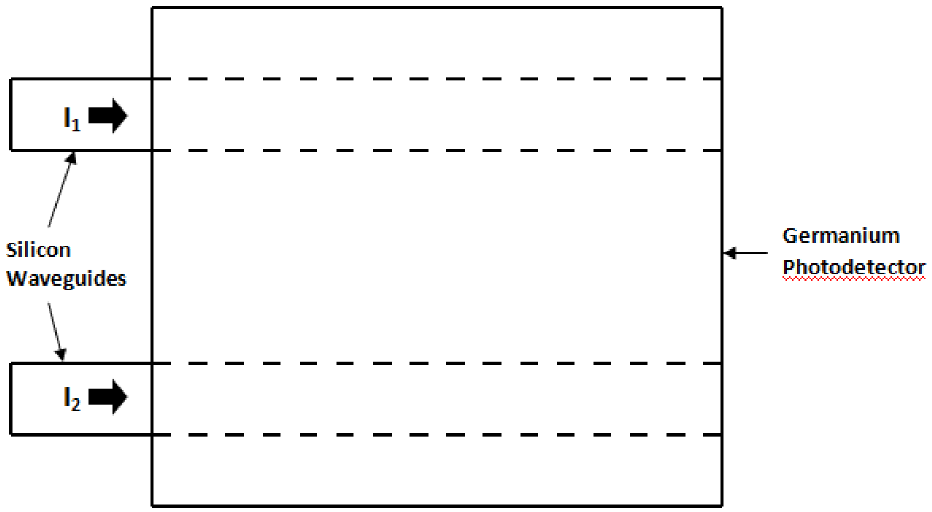

Figure 4.1. Schematic of germanium photodetector layer on top of the silicon waveguides. This model has zero tilt which will result in no phase error.

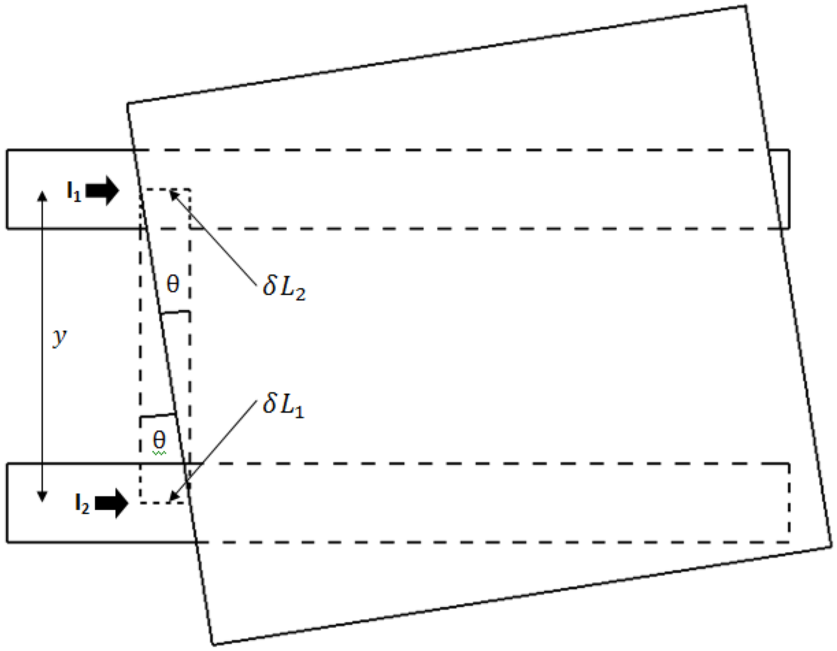

Figure 3.2. Schematic of germanium photodetector on top of the silicon waveguides with tilt angle θ.

The addition of phase error will result in the expression

$$I = I_1 - I_2 = 2R\sqrt{P_s P_{LO}}\cos[\varphi_s - \varphi_{LO} + \delta\varphi] \qquad (4.7)$$

$$I = 2R\sqrt{P_s P_{LO}}\cos[\varphi_s - \varphi_{LO} + (\delta\varphi_1 - \delta\varphi_2)] \tag{4.8}$$

where $\delta\varphi$ is the total phase error caused by phase terms $\delta\varphi_1$and $\delta\varphi_2$ coming from propagation in the two waveguides. These phase terms can be expressed by [21]

$$\delta\varphi_1 = \delta L_1 \beta_1 = y\beta_1 \tan\theta, \tag{4.9}$$

$$\delta\varphi_2 = \delta L_2 \beta_2 = y\beta_2 \tan\theta, \tag{4.10}$$

where y is the separation between the silicon waveguides beneath the germanium layer, $\delta L_1$and δL_2 are propagation distances based on tilt angle θ, and β_1 and β_2 are the propagation constants of each guided wave section. The propagation constants are obtained as the product of the vacuum wavenumber and effective refractive index of the waveguide section being propagated through [22]. For the silicon waveguide, the effective index and propagation constant were determined to be 2.858 and 1.23 x 10^7 m^{-1}, respectively. For the section of propagation containing germanium and silicon, the effective refractive index and propagation constant was determined to be 3.936 and 1.65 x 10^7 m^{-1}, respectively. The effective refractive indices were obtained through simulation using Optiwave software at 1.5 µm wavelength.

With these equations, Matlab was used to model the variation in photocurrent as a function of tilt angle. For this simulation, the local oscillator phase was assumed to be 0 while the signal phase was assumed to be π. A further assumption was made that a negative photocurrent would represent a 0 bit, while a positive photocurrent would represent a 1 bit. However, this is entirely arbitrary. Without any phase error, the selected local oscillator and signal phases will result in a negative photocurrent. The tilt angle was increased until the photocurrent changed from a negative to a positive value. This represented the maximum amount of tilt error that could be tolerated until a decision circuit would interpret a 0 bit incorrectly as a 1 bit due to a change in photocurrent polarity.

The maximum tilt angle was determined to be approximately 2.14°. This tilt tolerance should be easily obtainable during the fabrication process. This could be improved with a decrease in the separation distance between the silicon waveguides. However, this would lead to a decrease in electrode finger length which might be increasingly difficult to fabricate. Furthermore, the optical signal evanescently coupled into the germanium will expand beneath the electrode contact pads if the electrode fingers are too short.

4.2. MMI Power Splitting Ratio

If the output power from the MMI is not equally split down each of the silicon waveguides, the device will not be balanced. This will lead to relative intensity noise from the signal and local oscillator, contributing to the total photocurrent. We can model this by modifying eq. (6) to [23]

$$I = I_1 - I_2 = 2R\left(\frac{2\sqrt{b}}{1+b}\right)\sqrt{P_s P_{LO}(1+r_s)(1+r_{LO})}\cos[\varphi_s - \varphi_{LO}] \qquad (4.11)$$

where r_s and r_{LO} are the relative intensity noise of the signal and local oscillator, respectively. The parameter b represents how well balanced the device is, with b equal to 1 for perfect balance. If we assume a signal power of 100 µW and a local oscillator power of 1 µW, the RIN due to the signal will be negligible while the RIN due to the local oscillator will be ~0.01 [23]. With a responsivity of approximately 0.8 A/W, determined in section 3.2, the photocurrent was modeled against the balance parameter. Figure 4.3 depicts the dependence of the photocurrent on this parameter. As can be observed, there needs to be a relatively large amount of power imbalance before the total photocurrent is significantly affected.

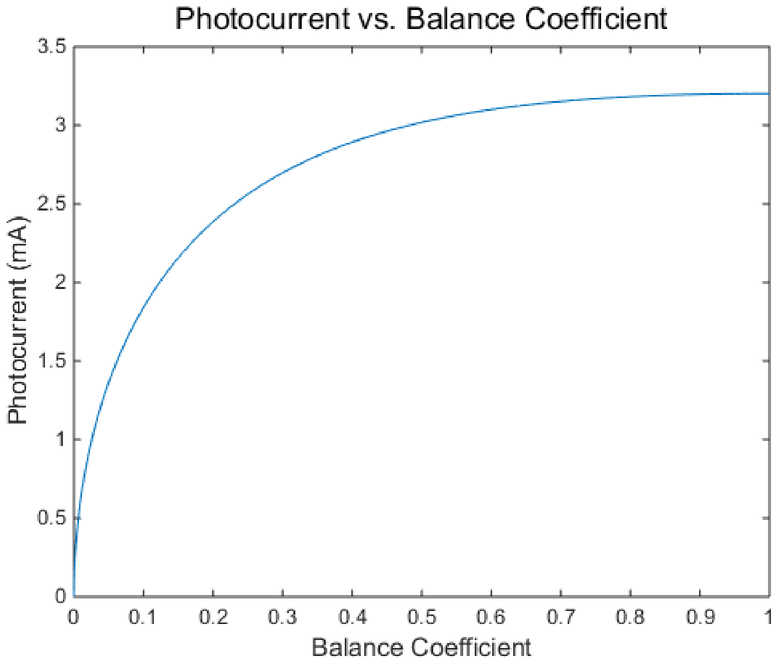

Figure 4.3. Photocurrent as a function of balance coefficient. This coefficient relates how well split the power is down each silicon waveguide. Ideally, the split would be 50%/50% for b=1. Note that there needs to be a relatively large amount of imbalance before the photocurrent exhibits a noticeable decline.

4.3. Interdigitated Electrode Alignment Error

Another source of error would be the misalignment of the interdigitated electrodes. The only parameter that a misalignment of electrodes would affect would be the capacitance of the photodetector. This was modeled in Matlab using electrode finger length and width of 4 µm and 0.5 µm, respectively. For the perfect alignment, the finger spacing was set at 0.5 µm for a finger period of 1 µm. This was compared against a 0.1 µm misalignment of the fingers (20%). This would result in two different periods of 0.9 µm and 1.1 µm, each over half the total area of the detector. As can be seen in Figure 4.4, a misalignment of 20% does not significantly affect the capacitance of the photodetector and thus this source of error should not be a major concern during fabrication.

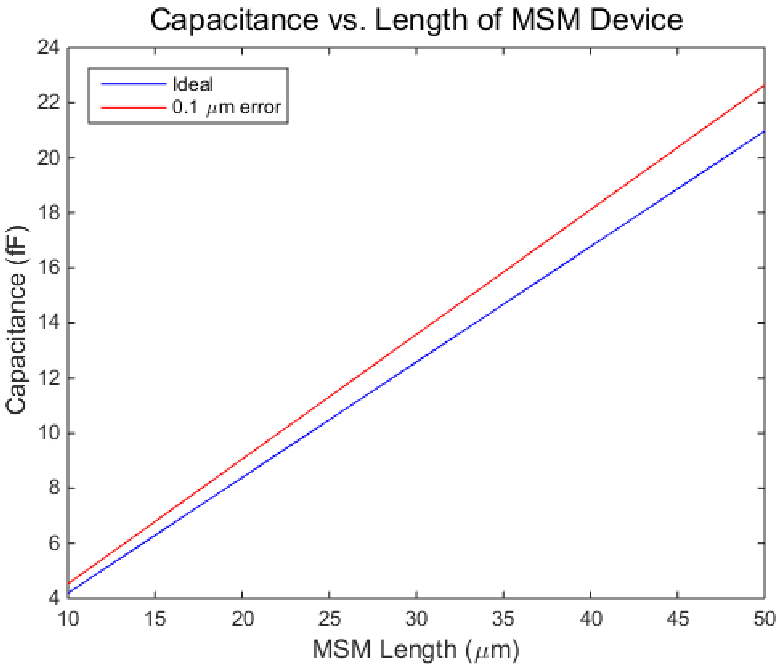

Figure 4.4. Capacitance vs. length of MSM photodetector. An electrode finger alignment error of 0.1µm was introduced, which results in two different periods of 0.9 and 1.1 µm. Note that 0.1 µm represents a 20% error, without resulting in any significant error in capacitance.

4.4. Lateral Optical Signal Expansion in Germanium Layer

Simulations were run to verify that the optical signal being evanescently coupled from the 0.5 µm wide silicon waveguide into the 4 µm wide germanium detector layer was not expanding wider than the length of the electrodes. If this occurs, the signal would be propagating along the germanium layer under the electrode contact pads, which would interfere with proper generation and extraction of electron-hole pairs. As can be observed in Figure 4.5, the optical signal is expanding to 4 µm width after approximately 32 µm of detector length. Since our photodetector will be approximately 40 µm in length, the optical signal will be propagating under the contact pads for 8 µm.

One solution would be to increase the width of the germanium detector layer. If we increase the width from 4 µm to 5 µm, the optical signal does not expand to the full width of the detector after 40 µm of propagation, as can be observed in Figure 4.6. Another solution would be to utilize a material that would act as a barrier to the expansion of the signal. However, this would add increased complexity to the fabrication of the device.

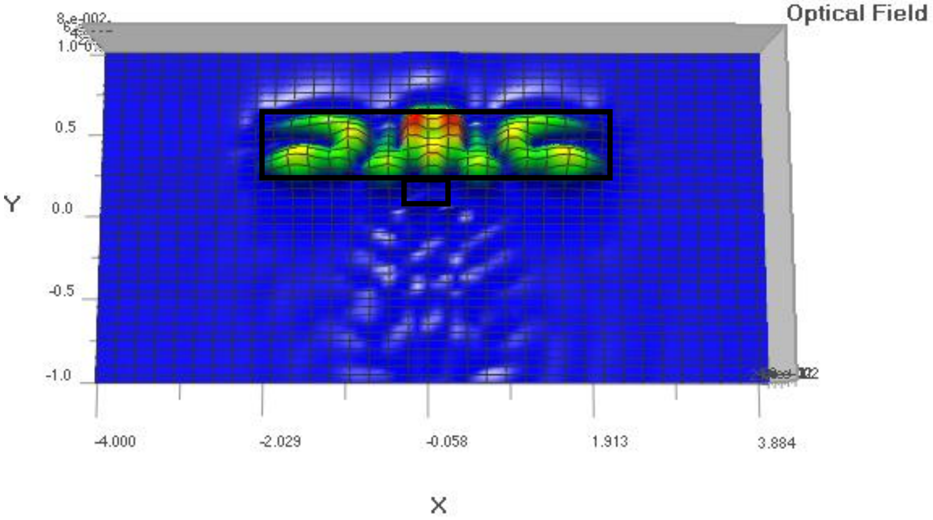

Figure 4.6. Optical field propagation along z-axis at MSM length of 32 µm. The field coupled into the 4 µm wide germanium layer has expanded to the edge at approximately 32 µm.

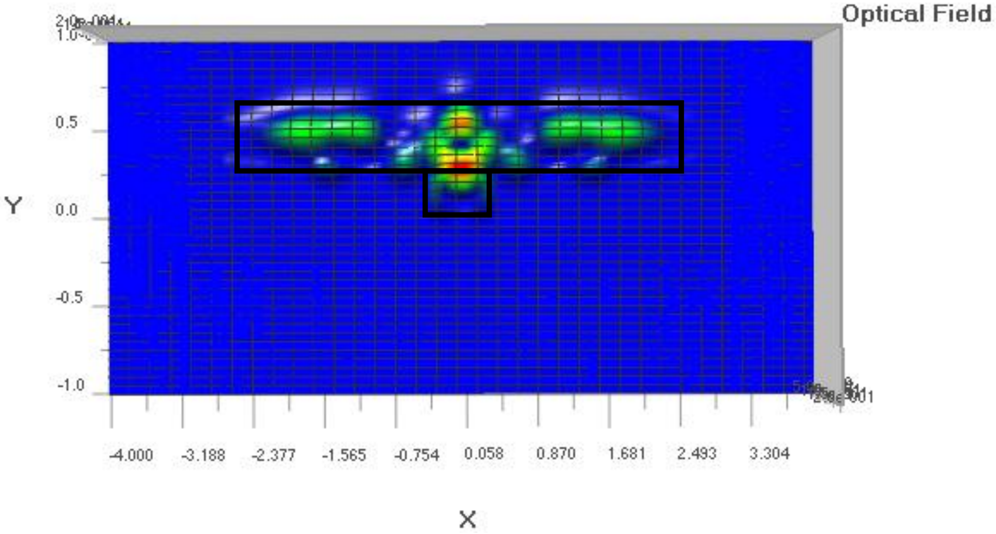

Figure 4.6.Optical field propagation along z-axis at MSM length of 50 µm. The width of the Ge layer has been increased to 5 µm to simulate electrode fingers of 5 µm. As you can observe, the field does not reach the boundary of the Ge layer.

5. PROPOSED FINAL DESIGN

5.1. Separation of MSM Photodetectors

The output waveguides from the MMI were designed to be 0.5 µm wide with a center-to-center separation distance only 1.0 µm (0.5 µm separation between exterior walls). This is clearly not enough space to wafer bond the MSM photodetectors to the surface. Therefore, we need to increase the separation of the output silicon waveguides without significant degradation of the optical signal. Using a gradual S-bend waveguide over a propagation distance of 30 µm, we can achieve 10 µm of separation between the waveguides while still maintaining the optical signal, as shown in Figure 5.1.

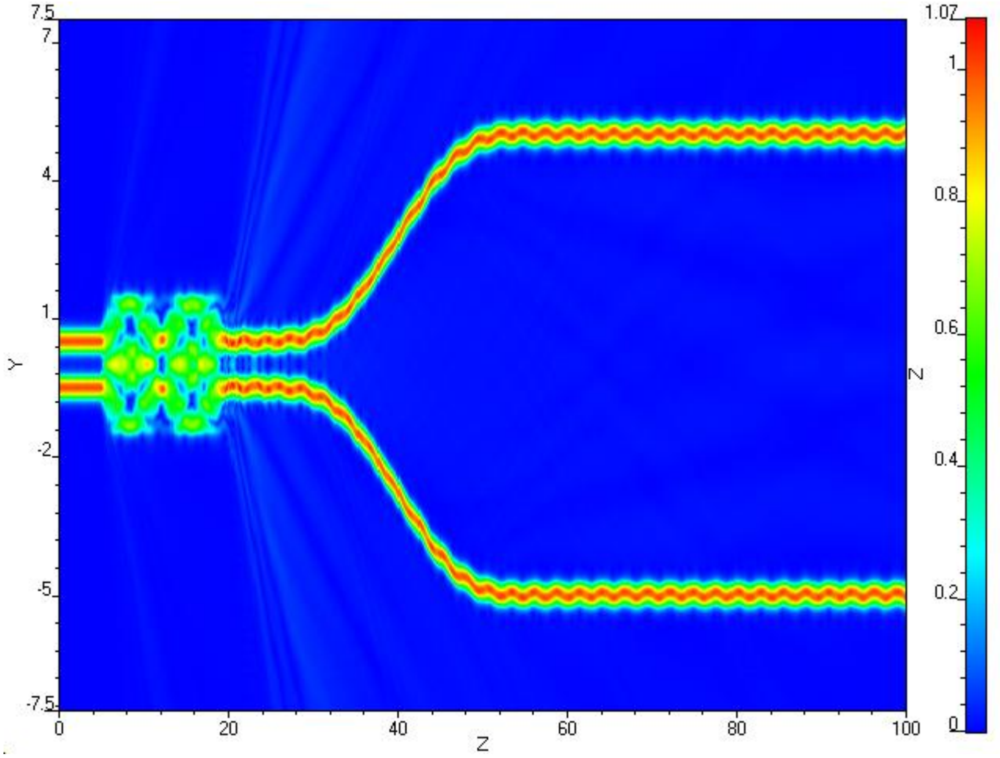

Figure 5.1. Single mode optical field propagation through the MMI structure. The output waveguides were bent away from each other to provide enough spacing for the interdigitated electrode fingers on the germanium layer that would be wafer bonded on top.

The trade-off is between how much separation we need versus how much tilt we can tolerate. As was alluded to in section 4.1, increasing the separation between the two waveguides will result in a reduction in the amount of tilt we can tolerate while still being able to properly detect in the phase of the signal. For this separation of 10 µm, we are able to tolerate up to approximately 2° of tilt, which is very reasonable considering the resolution of modern surface mount technology (SMT).

5.2. Schematics

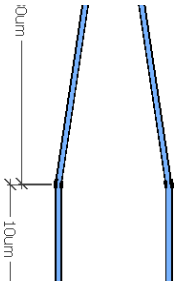

Figure 5.2. This is the final layout of the ultra-compact balanced coherent 2x2 MMI to MSM photodetector, roughly to scale.

6. PRELIMINARY FABRICATION

6.1. MMI

The MMI is fabricated in a multi-step photolithography process. The first step involved spin-coating a layer of ma-N2403, a negative E-beam resist made by micro resist technology GmbH, on our SOI wafer for 30 seconds at 1850 rpm, followed by baking the wafer on a hotplate at 90°C for 60 seconds. This resulted in a resist layer that was approximately 400 nm thick. We then cleaved a piece of the SOI wafer that was approximately 4 mm wide and 8 mm long. We placed this in an Elionix 7000 E-beam Lithography system and exposed the pattern of the MMI on the wafer. This EBL system is ideal for our application due to its ability to write device features as small as 10 nm with an acceleration voltage of 100 keV. Next we developed the pattern in ma-D525, also made by micro resist technology, for one minute. We immediately rinsed the wafer in deionized water, followed by a thorough air-drying using N_2 gas.

The next step in the fabrication process requires dry etching in an Oxford Instruments reactive ion etch system to etch away at the silicon wafer to define our MMI structure. To accomplish this, a gas mixture of 5 sccm 0_2 and 22 sccm CF_4 with a pressure of approximately 20 mTorr and power of 100 W was used for 5 minutes. After this was completed, the photoresist layer was removed. The fabricated MMI was then placed in an atomic force microscope for observation (see Figure 6.1).

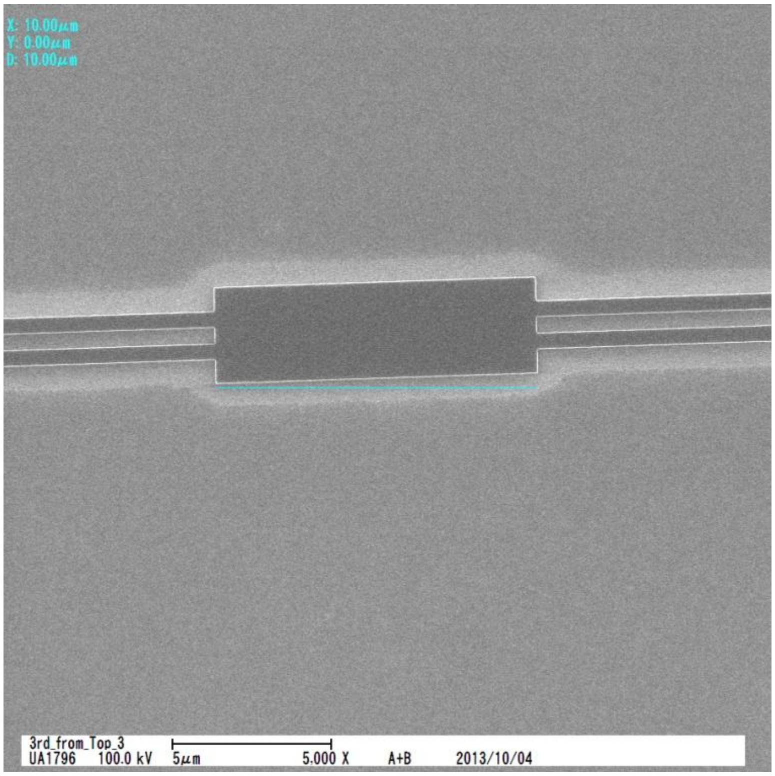

Figure 6.1. SEM image of the fabricated 2x2 MMI (courtesy of Michal Lukowski).

The primary device features appear to have been etched properly. However, we did not reach an etch depth of 220 nm for the waveguides and MMI, as required for proper operation. More work would need to be conducted to optimize the etch process by adjusting the gas combinations, power, or etch time.

6.2. Future Fabrication Work

Future work would need to be performed to fabricate the MSM photodetector. Ideally, a small piece of germanium wafer would need to be cleaved and placed in an e-beam deposition chamber. A thin layer of titanium followed by a layer of gold would be deposited. The wafer would then have a layer of photoresist spincoated on the gold surface and baked on a hot plate. The desired pattern of the electrodes would be exposed in the EBL and then etched using reactive ion etching. Finally, the excess photoresist would be removed and the wafer would be directly wafer bonded to the silicon waveguide outputs.

7. CONCLUSION

A novel approach for ultra-compact balanced coherent photodetection using silicon photonics was designed, simulated, and partially fabricated. The simulations demonstrate that the device can exhibit low capacitance, low dark current with proper Schottky barrier enhancement techniques, and large optical frequency. Furthermore, the length of the photodetection layer can easily be increased for greater responsivity and external quantum efficiency. Using a direct wafer bonding approach, the MMI and MSM can be fabricated separately and bonded to each other, effectively avoiding growth defects that can occur due to the large lattice mismatch between germanium and silicon. A simple model was also developed to determine the maximum amount of tilt tolerance allowed if surface mount technology is utilized for hybrid integration of the device.

ACRONYMS

MMI	Multi-mode interference device
MSM	Metal-semiconductor-metal photodetector
CMOS	Complementary metal-oxide semiconductor
SOI	Silicon-on-insulator
TiAu	Titanium-gold
SMT	Surface-mount technology

REFERENCES

1. M. Miura, J. Fujikata, M. Noguchi, D. Okamoto, T. Horikawa, and Y. Arakawa, "Differential receivers with highly-uniform MSM Germanium photodetectors capped by SiGe," Optics Express, Vol. 21, 23295-23306, (2013).
2. J. Fujikata, M. Miura, M. Noguchi, D. Okamoto, T. Horikawa, and Y. Arakawa, "Si waveguide-integrated metal-semiconductor-metal and p-i-n-type Ge photodiodes using Si-capping layer," Japanese Journal of Applied Physics, Vol. 52, 04CG10, (2013).
3. M. Rouvière, L. Vivien, X. Le Roux, J. Magneney, P. Crozat, C. Hoarau, E. Cassan, D. Pascal, S. Laval, J.-M. Fédéli, J.-F. Damlencourt, J.M. Hartmann, and S. Kolev, "Ultrahigh speed germanium-on-silicon-on-insulator photodetectors for 1.31 and 1.55 µm operation," Applied Physics Letters, Vol. 87, 231109, (2005).

4. L. Colace, G. Masini, F. Galluzzi, G. Assanto, G. Capellini, L. De Gaspare, E. Palange, and F. Evangelisti, “Metal-semiconductor-metal near-infrared light detector based on epitaxial Ge/Si,” Applied Physics Letters, Vol. 72, 3175, (1998).
5. W.-T. Chen, C.-K. Tseng, K.-H. Chen, H.-D. Liu, Y. Kang, N. Na, and M.-C. Lee, “Self-aligned microbonded germanium metal-semiconductor-metal photodetectors butt-coupled to Si waveguides,” IEEE Journal of Selected Topics in Quantum Electronics, Vol. 20, 3800605, (2014).
6. L. Chen, P. Dong, and M. Lipson, “High performance germanium photodetectors integrated on submicron silicon waveguides by low temperature wafer bonding,” Optics Express, Vol. 16, 11513-11518, (2008).
7. L. B. Soldano and E. C. M. Pennings, “Optical multi-mode interference devices based on self-imaging: principles and applications,” Journal of Lightwave Technology, Vol. 13, 615-627, (1995).
8. J. D. B. Soole and H. Schumacher, “InGaAs metal-semiconductor-metal photodetectors for long wavelength optical communications,” IEEE Journal of Quantum Electronics, Vol. 27, 737-752, (1991).
9. N. C. Harris, T. Baehr-Jones, A. E.-J. Lim, T. Y. Liow, G. Q. Lo, and M. Hochberg, “Noise characterization of a waveguide-coupled MSM photodetector exceeding unity quantum efficiency,” Journal of Lightwave Technology, Vol. 31, 23-27, (2013).
10. J. Kim, W. B. Johnson, S. Kanakaraju, W. N. Herman, and C. H. Lee, “Demonstration of balanced coherent detection using polymer optical waveguide integrated distributed traveling-wave photodetectors,” Optics Express, Vol. 17, 20242-20248, (2009).

11. Y. Painchaud, M. Poulin, M. Morin, and M. Têtu, “Performance of balanced detection in a coherent receiver,” Optics Express, Vol. 17, 3659-3672, (2009).
12. S. Chandrasekhar, B. Glance, A. G. Dentai, C. H. Joyner, G. J. Qua, and J. W. Sulhoff, “Monolithic balanced p-i-n/HBT photoreceiver for coherent optical heterodyne communications,” IEEE Photonics Technology Letters, Vol. 3, 537-539, (1991).
13. L. Y. Lin, M. C. Wu, T. Itoh, T. A. Vang, R. E. Miller, D. L. Sivco, and A. Y. Cho, “High-power high-speed photodetectors – design, analysis, and experimental demonstration,” IEEE Transactions on Microwave Theory and Techniques, Vol. 45, 1320-1331, (1997).
14. Pallab Bhattacharya, Semiconductor Optoelectronic Devices, Prentice Hall, (1997).
15. D. Ahn, C.-Y. Hong, J. Liu, W. Giziewicz, M. Beals, L. C. Kimerling, and J. Michel, “High performance, waveguide integrated photodetectors,” Optics Express, Vol. 15, 3916-3921, (2007).
16. S. Demiguel, N. Li, X. Li, X. Zheng, J. Kim, J. C. Campbell, H. Lu, and A. Anselm, “Very high-responsivity evanescently coupled photodiodes integrating a short planar multimode waveguide for high-speed applications,” IEEE Photonics Technology Letters, Vol. 15, 1761-1763, (2003).
17. W. A. Wohlmuth, P. Fay, and I. Adesida, “Dark current suppression in GaAs metal-semiconductor-metal photodetectors,” IEEE Photonics Technology Letters, Vol. 8, 1061-1063, (1996).
18. K.-W. Ang, S.-Y. Zhu, J. Wang, K.-T. Chua, M.-B. Yu, G.-Q. Lo, and D.-L. Kwong, “Novel silicon-carbon (Si:C) schottky barrier enchancement layer for dark-current suppression

in Ge-on-SOI MSM photodetectors," IEEE Electron Device Letters, Vol. 29, 704-707, (2008).

19. A. Xiang, W. Wohlmuth, P. Fay, S.-M. Kang, I. Adesida, "Modeling of InGaAs photodetector for circuit-level simulation," Journal of Lightwave Technology, Vol. 14, 716-723, (1996).
20. J. Burm, K. I. Litvin, W. J. Schaff, and L. F. Eastman, "Optimization of high-speed metal-semiconductor-metal photodetectors," IEEE Photonics Technology Letters, Vol. 6, 722-724, (1994).
21. T. Goh, S. Suzuki, and A. Sugita, "Estimation of waveguide phase error in silica-based waveguides," Journal of Lightwave Technology, Vol. 15, 2107-2113, (1997).
22. Rüdiger Paschotta, "Effective refractive index," RP Photonics, http://www.rp-photonics.com/effective_refractive_index.html.
23. S. S. Agashe, S. Datta, F. Xia, and S. R. Forrest, "A monolithically integrated long-wavelength balanced photodiode using asymmetric twin-waveguide technology," IEEE Photonics Technology Letters, Vol. 16, 236-238, (2004).
24. Govind P. Agrawal, Fiber-Optic Communication Systems, Wiley, (2002).